32nd URSI GASS, Montreal, 19–26 August 2017

Radiative Transfer in Turbulent Flow using Spacetime Discontinuous Galerkin Finite Element Method

Saba Mudaliar*(1), Phillip Clarke(2) and Reza Abedi(2)
(1) Sensors Directorate, Air Force Research Laboratory, Wright-Patterson AFB, Dayton, OH 45433, saba.mudaliar@us.af.mil
(2) University of Tennessee Space Institute (UTSI), Tullahoma, TN, 37355, www.rezaabedi.info, rabedi@utsi.edu

Abstract

The radiative transfer equation for a problem that involves scattering, absorption and radiation is solved using spacetime discontinuous Galerkin (SDG) method. The strength of finite element method to handle scattering problems in heterogeneous media with complex geometries is well known. Adaptive operations in spacetime facilitates very accurate and efficient solution algorithm. We investigated the accuracy of the SDG method by using the method of manufactured solutions. For the case of harmonic phase functions we illustrate how the L2 norm error decreases with the choice of high order polynomial and more refined element size. Key merits of the use of SDG for our problem enamates from its linear solution cost, and the ability to obtain the solution for a wide frequency spectrum in one time domain simulation.

1 Introduction

Several techniques exist for wave propagation through turbulent flows. Although such flows can be well described by Navier-Stokes equations, any further understanding of the characteristics of the flow is quite difficult. Even direct numerical simulations do not help, provided one takes a statistical perspective. Wave propagation through such a flow is then described by a stochastic differential equation. Perhaps the simplest and most intuitive method to solve such a problem is the radiative transfer approach [1, 2] in the mesoscopic limit. Here one seeks the solution for the second moment of the wave function. An important merit of the RT approach is that all the key parameters of the equation are measureable quantities. This is the main reason that the RT approach is very popular in numerous disciplines. For our application, the RT approach is most appropriate because it offers a unified framework under which, scattering, emission and absorption are incorporated in a self-consistent manner.

There exist in the literature numerous algorithms for solving RT equations. Most of them are applicable to plane parallel geometries [3], [4] under frozen turbulence assumption. In contrast, our problem is truly three-dimensional. Analytical solutions of RT equations is available only in a few simple problems. For most others, one has to resort to numerical algorithms. Among the classical numerical methods available, the finite element method is most appropriate because of its ability to deal with complex geometries and heterogenous media. In our application, the dimension of the flow region is very large in terms of signal wavelength. A multitude of scales of fluctuation is involved in the flow region. Also, the scales of fluctuations and have a large spatial variation. Also, note that it is very expensive to carry out classical FEM computation for wave propagation of a wide band signal through the flow. In view of all these facts we have employed a space-time discontinuous Galerkin method [5] for our problem.

2 Radiative Transfer Formulation

Radiative transfer theory provides a simple and unified framework for self-consistently incorporating scattering, absorption, and emission in the flow problem. In this formulation, the radiant intensity is governed by the following radiative transfer equation:

$$\hat{s}\cdot\nabla\boldsymbol{I}(\vec{x},\omega,\hat{s})+\Big[\boldsymbol{\eta}_s(\vec{x},\omega,\hat{s})+\boldsymbol{\eta}_a(\vec{x},\omega)\Big]\boldsymbol{I}(\vec{x},\omega,\hat{s})$$
$$-\vec{S}(\vec{x},\omega,\hat{s})-\int_{\hat{s}}\bar{\boldsymbol{P}}(\vec{x},\omega,\hat{s}\leftarrow\hat{s}')\boldsymbol{I}(\vec{x},\omega,\hat{s}')\,\mathrm{d}s'=0, \quad (1)$$

where the unknown vector $\boldsymbol{I}$ includes the radiation intensity, $\boldsymbol{\eta}_s$ and $\boldsymbol{\eta}_a$ are the material dependent scattering and absorption coefficients respectively, $\vec{S}$ is the emission term, and $\bar{\boldsymbol{P}}$ is the scattering phase function. Since the numerical solver that will be able to tackle this general equation is to be developed in stages, this work will focus on the scalar version of the above equation with rectangular geometry which is as follows:

$$\mu\cdot\nabla_z I(z,\mu)+\eta I(z,\mu)-S(z,\mu)$$
$$-\int_{-1}^{1}\bar{P}(z,\mu\leftarrow\mu')I(z,\mu')\,\mathrm{d}\mu'=0. \quad (2)$$

where the coefficient $\boldsymbol{\eta}$ is the summation of the absorption and scattering coefficient (i.e. $\eta=[\eta_a(\mu)+\eta_s(z,\mu)]$) for brevity.

3 Discontinuous Galerkin Weighted Residual

The finite element method is used to approximate the intensity I through the definition $I^h=\boldsymbol{H}_{1\times n}\cdot\boldsymbol{a}_{n\times 1}$, where $\boldsymbol{H}$

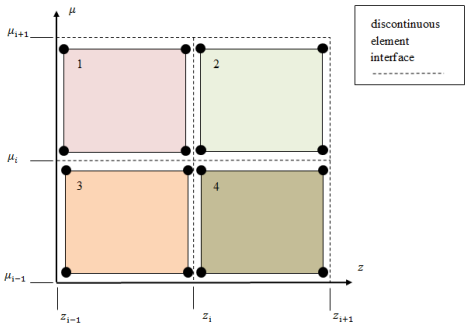

Figure 1. 1D Discontinuous Meshing

is a vector of basis functions and $\boldsymbol{a}$ are coefficients of unknown values. The above RTE can then be discretized over a finite element domain. It is important to note two main differences between the conventional Galerkin and discontinuous Galerkin methods as it relates to how discretization is carried out henceforth. The conventional FEM utilizes nodal type degrees of freedom (dof) with continuity of dof solutions being enforced. The value at each dof a_i is the value of the underlying unknown, *e.g.,* I, at the coordinate corresponding to that dof location. For example, in figure 1 the black solid circles correspond to where element nodes for a continuous FEM would have been located. All nodes at one position have the same value for I. For instance, at coordinate (z_i, μ_i) the value of I is the same for all four elements at that corner. The nodal continuity of continuous FEMs dictates the form of shape function $\boldsymbol{H}$. Due to continuity requirement and noting $I^h = \boldsymbol{H}_{1\times n} \cdot \boldsymbol{a}_{n\times 1}$, H_i takes the value of unity at element node i and zero at other nodes.

For DG methods, the element continuity is not enforced at element nodes. This concept is visualized in figure 1. Continuity for DG methods are built in through the enforcing of 'jump conditions' across element interfaces. For an n^{th} order approximation, the components of the shape functions H_i are chosen such that they span the space of n^{th} order polynomials. An example of this concept can be seen using a 2D quadrilateral DG element. For a linear element the solution at any location $\vec{x} = (x_1, x_2)$ within the discontinuous Galerkin element is then $w_e^h(\vec{x}) = a_0 + a_1 x_1 + a_2 x_2 + a_3 x_1 x_2$.

4 FEM Formulation

The weighted residual (WR) of the finite element formulation is formed by expressing the solution $I(z,\mu) = \boldsymbol{H}(z,\mu)\boldsymbol{a}$ and multiplying the partial differential equation (PDE) (2) by the weight function $\hat{\boldsymbol{H}}$.

$$R = \int_\Omega \hat{\boldsymbol{H}} \Big[\mu \cdot \partial_z(\boldsymbol{H}\cdot\boldsymbol{a}) + [\eta_a(\mu) + \eta_s(z,\mu)]\boldsymbol{H}\cdot\boldsymbol{a} - S(z,\mu) - \int_{-1}^{1} \bar{P}(z,\mu \leftarrow \mu')(\boldsymbol{H}\cdot\boldsymbol{a})' \, \mathrm{d}\mu' \Big] \, \mathrm{d}A + \int_{\partial\Omega} \hat{\boldsymbol{H}} \Big(I^* - (\boldsymbol{H}\cdot\boldsymbol{a}) \Big) \hat{n}_z \, \mathrm{d}X = 0. \quad (3)$$

where Ω and $\partial\Omega$ are the interior and the vertical boundaries (at $z = [z_{min}, z_{max}]$), respectively. The term $(I^* - I)\hat{n}_z = (I^* - (\boldsymbol{H}\cdot\boldsymbol{a}))\hat{n}_z$ is the previously mentioned jump condition which enforced the continuity between each element; the jump condition is imposed on all *vertical* (constant z) element interfaces. This equation can then be written on an element-wise basis using a Gauss quadrature coordinate system to perform numerical integration for a simple quadrilateral. To construct that linear system of equations that will be solved the above weighted residual is solved element-wise and all *stiffness* type terms (terms dependent of unknown coefficient vector $\boldsymbol{a}$) and *force* type terms (terms independent of unknown coefficient vector) and placed into their global correspondents. Each of the above terms are placed into a local stiffness and force tensor which is then transferred to a global stiffness $\underline{K}$ and force $\boldsymbol{F}$ tensor for the system on form:

$$\underline{K}\boldsymbol{a} = \boldsymbol{F}. \quad (4)$$

For K_{ij}, the indices i, j represent a block matrix within the tensor K that is a result of the outer product of shape function for element i and element j (i.e. $K^{ij}_{(n\times m)} = H^i_{(1\times n)} \otimes H^j_{(1\times m)}$).

5 Method of Manufactured Solution

Verification of the code is carried out using the procedure known as Method of Manufactured Solution (MMS). MMS assumes a known function form (exact solution) such that $I(z,\mu) = f(z,\mu)$. This assumed exact solution is then imposed into the 1D RTE which is transposed to determine a form of the source term S. This source term then is used within the FE implementation.The boundary conditions are also defined as being exactly the assumed exact solution $I(z,\mu) = f(z,\mu)$ at boundary coordinates $(z^{\partial\Omega}, \mu)$. Assuming $f(x)$ is a polynomial belongs to discrete solution space, the FE solution $I^h(z,\mu)$ should recapture the solution given by $f(z,\mu)$. However, due to finite precision errors there will be very small discrepancies between the two solutions that depend on machine precision. In the following examples, the two solutions are compared point-wise with a relative tolerance of $\varepsilon = 1E-6$. All the test cases below share the same spatial(1D)×angle mesh(1D) mesh. It is important to note that each spatial layer $z^{[i]}$ and angle layer $\mu^{[i]}$ are subdivided into three bands (elements) and each layer is assigned different and independent material properties $(\eta_a^{[i]}, \eta_s^{[i]})$ to ensure discontinuity in layers for code verification. Utilizing this setup, the two cases are characterized by a zero and non-zero Phase function $\bar{P}(z,\mu \leftarrow \mu')$ within equation 2 respectively. For simplicity, the assumed exact solutions are only distinguished by angular layers; all spatial layers within a given angular layer will be assigned the same exact solution based on this angular layer.

Test case for $\bar{P}(z,\mu \leftarrow \mu') \neq 0$
For a nonzero phase function equation 2 can be rewritten in

terms of the source $S(z,\mu)$ as:

$$S(z,\mu) = \mu \cdot \nabla_z I(z,\mu) + \eta I(z,\mu) - \int_{-1}^{1} \bar{P}(z,\mu \leftarrow \mu') I(z,\mu')\, \mathrm{d}\mu'. \quad (5)$$

The prescribed Phase function used in this case is of the following polynomial form with z, μ, and μ' orders 2, 1, and 2, respectively:

$$\begin{aligned}\bar{P}(z,\mu \leftarrow \mu') =& 4.0 + 4.2*z + 11.2*z^2 - 10.3*\mu + 4.0\mu*z \\ &+ 3.3*\mu*z^2 - 3.1*\mu' + 2.5*\mu'*z + 4.1*\mu'*z^2 \\ &- 5.1*\mu*\mu' - 2.6*\mu*\mu'*z + 1.3*\mu*\mu'*z^2 \\ &- 1.6*\mu'^2 + 2.1*\mu'^2*z - 12.1*\mu'^2*z^2 \\ &- 15.2*\mu*\mu'^2 - 7.8*\mu*\mu'^2*z - 2.5*\mu*\mu'^2*z^2\end{aligned}$$

For this more complex problem, each angle layer $\mu^{[i]}$, for $i = 1, \cdots, 4$ is assigned identical assumed exact solution of the following polynomial form:

$$\begin{aligned}I^{[i]} =& f^{[i]}(z,\mu) = 4.0 + 4.2*z + 11.2*z^2 - 10.3*\mu + 4.0*z*\mu \\ &+ 3.3z^2*\mu - 3.1*\mu^2 + 2.5*z*\mu^2 + 4.1z^2*\mu^2, \text{ for } i = 1,..,4\end{aligned}$$

For this case all elements in the spatial layers j and in the angular layers i are interpolated with second order basis $k = 2$ for $z^{[j]}$,and $k = 2$ for $\mu^{[i]}$ respectively. With the above exact solution forms and their corresponding source terms defined by equation 5, the following solution is generated as visualized in figure 2.

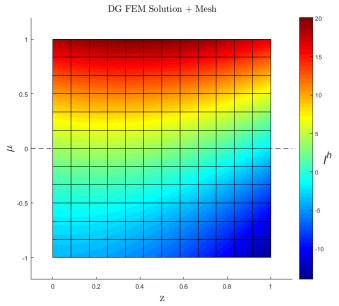

Figure 2. Visualization of solution for code verification case of non-zero phase function

6 Convergence Study

Utilizing the above method of manufactured solution an error analysis can be performed to ensure that the numerical solution convergences to the exact solution and to obtain the corresponding convergence rate. We use the L2 norm of the point-wise error $\mathscr{E}$ between the discrete and the exact solution to characterize numerical error,

$$\text{point-wise error: } \mathscr{E} = I^h(z,\mu) - I^{exact}(z,\mu)$$

$$\text{L2 norm of error: } L^2(\mathscr{E}) = \sqrt{\int_\Omega ||\mathscr{E}||^2 \, \mathrm{d}\Omega}$$

$$= \sqrt{\int_\Omega (I^h(z,\mu) - I^{exact}(z,\mu))^2 \, \mathrm{d}\Omega}.$$

For the exact solution of a polynomial form, it is sufficient to evaluate the absolute error at arbitrary points within each finite element to realize that the numerical solver is able to capture the exact solution. The error generated in this case is dominated by that due to finite precision; this error is dependent on the computational machine and is on an order of magnitude that is essentially negligible. For the case of a non-polynomial form (e.g. harmonic form) exact solution, the error induced by finite precision is negligible compared to discretization error.

The convergence of the solution generated by the numerical solver is simply verified by determining the slope β^p of the linear equation derived from interpolation of a data set of refined element size ($\frac{h}{n}$, $n = 1,..,\infty$) and average error value pairs on a logarithmic scale. For a specific element interpolation polynomial order p, the convergence rate (the slope) should be equal to the value of the polynomial order plus one (i.e. $\beta^{p+1} = p$) for this problem and L2 error norm.

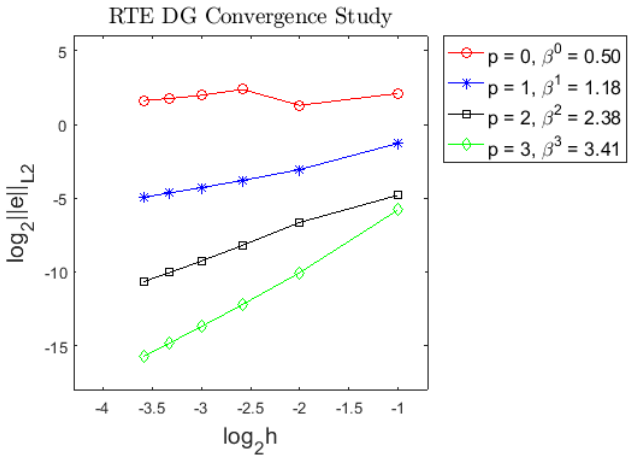

Figure 3. Convergence study for harmonic exact solution and harmonic Phase Function; $\bar{P}(z,\mu \leftarrow \mu') \neq 0$

Figure 3 shows a convergence study outcome utilizing an exact solution and phase function both of harmonic forms given as:

$$I^{exact}(z,\mu) = sin(\pi\frac{z}{L}) * sin(\pi\mu)$$

$$\bar{P}(z,\mu \leftarrow \mu') = \eta_s(z,\mu) * cos((\mu - \mu')\frac{\pi}{2})$$

,where L is the length of the element in the spatial z coordinate direction. The solution is seen to be convergent as the slope of each linear interpolation matches the basis order used to generate the numerical solution.

7 Point source implementation

The solver was implemented with the capability to have point sources $S_I(\bar{z},\bar{\mu})$ both on the boundary and interior of

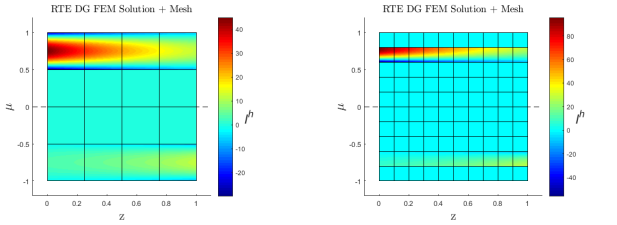

(a) Boundary point source for 4×4 mesh

(b) Boundary point source for 10×10 mesh

Figure 4. Radiation from a Point Source on the Boundary

the domain. For a source term at point $(\bar{z}, \bar{\mu})$, the source term value at any arbitrary point within the computational domain at point (z, μ) with respect to the reference source can be written as:

$$S(z,\mu) = S_I(\bar{z},\bar{\mu})\delta(z-\bar{z})\delta(\mu-\bar{\mu}) \tag{6}$$

where $S_I(\bar{z},\bar{\mu})$ is the intensity of the point source.

Recall the weighed residual term containing the source term:

$$\int_0^1 \Delta z \int_0^1 \Delta\mu S(z,\mu)\hat{\boldsymbol{H}}(\xi_z,\xi_\mu)\, \mathrm{d}\xi_\mu\, \mathrm{d}\xi_z$$

substituting equation 6 into this weighted residual terms yields the following:

$$\int_0^1 \Delta z \int_0^1 \Delta\mu \hat{\boldsymbol{H}}(\xi_z,\xi_\mu) S_I(\bar{z},\bar{\mu})\delta(z-\bar{z})\delta(\mu-\bar{\mu})\, \mathrm{d}\xi_\mu\, \mathrm{d}\xi_z$$

which further simplifies into a term that contributes to the global force tensor as

$$F = \hat{\boldsymbol{H}}(\xi_z,\xi_\mu) S_I(\bar{z},\bar{\mu})$$

evaluated within elements that contain the global point $(\bar{z},\bar{\mu})$. An example of the point source addition was performed in which the point source was placed on the left boundary of the domain and was of magnitude 10, specifically

$$S_I(\bar{z},\bar{\mu})(0.00, 0.75) = 10.$$

The left boundary was subject to a vacuum (homogeneous) boundary condition,

$$I(0.00,\mu)\cdot\hat{n}_z = 0$$

and the right boundary was subject to a reflective boundary condition,

$$I(1.00,-\mu)\cdot\hat{n}_z = I(1.00,\mu)\cdot\hat{n}_z.$$

the scattering coefficient $\eta_s(z,\mu)$ was defined to be zero for the domain resulting in a zero phase function value. The results of this example can be seen in figure 4.

An issue that can be seen here is about the point source location, one that is common within finite element implementation, is error due to numerical overshoot and undershoot near the point source. This error could be mollified by such means as imposing artificial diffusion but we find that refining the mesh results in the error being localized and negligible.

8 Conclusions

Wave propagation through turbulent flow that involves scattering, absorption, and radiation is a complex problem. A statistical approach is quite appropriate for such problems. When the wavelength is much larger than the turbulence scale, but small compared to the propagation size of the problem, the radiative transfer theory offers a simple and efficient representation of the physical processes. This equation describes the dynamics of the second moment of the radiation intensity in phase space. Our problem has multiple scales and complex geometries and heterogeneities. We employed the space-time discontinuous Galerkin method to solve this problem. This method offers a fast and accurate solution to our problem. We demonstrated the accuracy and convergence of our algorithm using the method of manufactured solutions. Although the problem taken for illustration is relatively simple the benefits of our algorithm will be more pronounced for more complex problems. We will demonstrate this by considering more complex geometries at the conference.

9 Acknowledgements

The authors thank AFOSR and NSF for support.

References

[1] V. I. Tatarskii. *The Effects of the Turbulent Atmosphere on Wave Propagation*. Israel Program for Scientific Translations, 1971.

[2] A. Ishimaru. *Wave Propagation and Scattering in Random Media*. Wiley-IEEE Press, 1999.

[3] S. Chandrasekhar. *Radiative Transfer*. Dover Publications, 1960.

[4] G.E. Thomas and K. Stamnes. *Radiative Transfer in the Atmosphere and Ocean*. Cambridge University Press, 1999.

[5] R. Abedi, S.T. Miller, R.B. Haber, and O. Omidi. Efficiency of high order methods in space and time: Study of elastodynamics problem using spacetime discontinuous Galerkin finite element method. 13th U.S. National Congress on Computational Mechanics (USNCCM13), University of California, San Diego, San Diego, CA, USA, July 26-30, 2015.